J Therm Spray Tech (2026) 35:549–562
https://doi.org/10.1007/s11666-026-02208-3

ORIGINAL RESEARCH ARTICLE

Microstructure and Tribological Behavior of TiN/ Al_2O_3 Composite Coatings Produced by High-Velocity Suspension Flame Spraying (HVSFS)

Ebru Gyoktepeliler Akin[1] · Luca Bortolotti[2] · Edoardo Rossi[3] · Milena Pazzi[2] · Andreas Killinger[1] · Luca Lusvarghi[2] · Giovanni Bolelli[2]

Submitted: 4 July 2025 / in revised form: 31 January 2026 / Accepted: 10 March 2026 / Published online: 24 March 2026

Abstract In this study, an aqueous suspension containing fine aluminum oxide and coarser titanium nitride (TiN) powders was prepared and processed using high-velocity suspension flame spraying (HVSFS) to produce thick TiN/ Al_2O_3 composite coatings (>50 µm). The influence of spraying parameters, such as total gas flow and flame stoichiometry, on the microstructure, phase composition, mechanical, and tribological properties was investigated. The results demonstrate that TiN can be successfully deposited under atmospheric conditions using the HVSFS process, achieving a homogeneous distribution of TiN particles within the alumina matrix. This composite structure led to a significant increase in microhardness. Furthermore, the TiN/ Al_2O_3 coatings produced with $\lambda = 0.8$ exhibited improved wear resistance and a reduced coefficient of friction compared to pure Al_2O_3 coatings.

Keywords HVSFS · S-HVOF · suspension spraying · thermal spraying · TiN coating · TiN/Al_2O_3 composite coating · tribology

Introduction

Several types of covalent and interstitial nitrides combine stability at high temperatures with high hardness, good wear resistance, and high durability against aggressive chemicals (Ref 1, 2). Titanium nitride (TiN) is one of the most widely used nitrides in the form of thin films as wear-resistant coatings for cutting tools, dielectric barriers, or electrodes in microelectronics (Ref 2). Conventional deposition methods such as physical vapor deposition (PVD) or chemical vapor deposition (CVD) are typically used to fabricate TiN coatings (Ref 3, 4). However, these methods are limited in terms of achievable coating thickness (<10 µm) and the size of the components that can be coated.

To overcome these limitations, thermal spraying offers an alternative with several advantages, such as higher deposition rates, localized application, and greater process flexibility. Nevertheless, the thermal spraying of TiN remains challenging due to its high oxidation sensitivity and the absence of a congruent melting point. Research efforts have therefore focused on in situ TiN formation via reactive plasma spraying (Ref 5). For instance, Bacci et al. (Ref 6) demonstrated the fabrication of thick Ti-TiN composite coatings by varying the Ar/N_2 gas ratio, which influenced the TiN content and improved hardness, albeit

This article is an invited paper selected from presentations at the 2025 International Thermal Spray Conference, held May 5–8, 2025, in Vancouver, 1 Canada, and has been expanded from the original presentation. The issue was organized by Giovanni Bolelli, University of Modena and Reggio Emilia (Lead Editor); Fardad Azarmi, North Dakota State University; Sara Bagherifard, Politecnico di Milano; Partha Pratim Bandyopadhyay, Indian Institute of Technology, Kharagpur; Šárka Houdková, University of West Bohemia; Heli Koivuluoto, Tampere University; Yuk-Chiu Lau, General Electric Power (Retired); Hua Li, Ningbo Institute of Materials Technology and Engineering, CAS; Sinan Müftü, Northeastern University; and Filofteia-Laura Toma, Fraunhofer Institute for Material and Beam Technology.

✉ Ebru Gyoktepeliler Akin
ebru.gyoktepeliler-akin@ikmt.uni-stuttgart.de

[1] Institute for Ceramic Materials and Technologies, University of Stuttgart, Stuttgart, Germany

[2] Department of Engineering "Enzo Ferrari", University of Modena and Reggio Emilia, Modena, Italy

[3] Department of Civil Engineering, Computer Science and Aeronautical Technology, University of Roma Tre, Rome, Italy

with noticeable porosity. Similarly, Feng et al. (Ref 7) enhanced the nitridation of titanium powder by adding nitrogen to the plasma, resulting in TiN-rich coatings with good wear resistance and lower friction compared to uncoated steel. Jing et al. (Ref 8) used reactive HVOF spraying with nitrogen as the feeding gas to produce coatings containing various TiN and oxide phases, achieving excellent corrosion resistance and wear reduction.

Unlike these in situ approaches, the present study uses pre-synthesized TiN powder dispersed in an aqueous suspension, enabling higher retention of the stable TiN phase and improved mechanical and chemical properties of the coating. Nevertheless, the above-mentioned issues related to high oxidation tendency under atmospheric conditions and decomposition before the melting point must be addressed to process a pre-synthesized TiN feedstock.

Sun et al. (Ref 9) investigated a TiN/TiO_2 composite coating using high-velocity suspension flame spraying (HVSFS), with TiN powder dispersed in a suspension. In their work, partial oxidation of TiN particles to TiO_2 was utilized to create a composite structure with embedded TiN particles, resulting in 11.2% retained TiN in the coating. Similarly, in our prior research on aluminum nitride (AlN) coatings via HVSFS, approximately 50% of the original nitride phase was preserved (Ref 10).

Another approach to spray nitrides is the use of a chemically compatible matrix material to partially retain the nitride phase while enhancing the overall coating properties. In this study, alumina (α-Al_2O_3) is employed as a matrix material and is dispersed together with TiN in an aqueous suspension. The thermal expansion coefficient of α- Al_2O_3 (CTE: 6.5–8.9 $\times$ 10^{-6} K^{-1}) (Ref 11) closely matches that of TiN (9.4 $\times$ 10^{-6} K^{-1}) (Ref 12), which helps minimizing the residual stress in the coating.

The HVSFS technique is suitable for fine ceramic powders (<5 µm), enabling the production of dense coatings with excellent mechanical properties such as high hardness and good adhesion strength (Ref 13-15). The flame temperature can reach up to 3000 °C, when using ethene as a fuel gas. Using water as the suspension medium helps lowering the flame temperature, thereby reducing the degradation of TiN particles during flight.

In this study, both pure alumina and a mixture of titanium nitride and alumina suspensions were sprayed using the HVSFS process. The influence of the spraying parameters, specifically the flame temperature (controlled by the ratio of combustion gas and oxygen) and the particle velocity (controlled by varying the total gas amount), was investigated with respect to the resulting microstructure, chemical and phase composition, and microhardness. Subsequently, the wear resistance of pure Al_2O_3 (as a reference) and TiN/Al_2O_3 composite coatings was evaluated and compared.

Materials and Methods

Feedstock Preparation

Commercially available Al_2O_3 (Martoxid MR52, Huber-Martinswerk, Germany) and TiN (Grade A, Höganäs, Sweden) powder were used to fabricate the suspensions. Detailed characterization of the feedstock was performed to verify the manufacturer´s specifications and obtain accurate baseline values for suspension stability and coating parameters. The morphology of the raw powders was examined using SEM. Titanium nitride (TiN) exhibits irregularly shaped particles, whereas the aluminum oxide (Al_2O_3) powder contains sub-micrometric particles, which tends to agglomerate (Fig. 1). As shown by the particle size distributions (Fig. 2), the TiN powder had a significantly larger average size (D_{50} = 8.6 μm) compared to Al_2O_3 (D_{50} = 1.9 μm), while both displayed a bimodal distribution.

Accordingly, the solid content of both suspensions was set to 15 wt.% and water (distilled H_2O) was used as a liquid medium. To prepare the pure Al_2O_3 suspension as reference, polymethacrylic acid was first added to the water medium at 1.7 wt.% based on the solid content. For TiN/Al_2O_3 suspension, a hydrocolloid was added first as a rheology agent at 4 wt.% relative to the water content and dissolved with a disperser (Dispermat, VMA-Getzmann GmbH, Germany) using a 70-mm-diameter dissolver disc at 500 rpm for 30 min. Then, synthetic polymethacrylic acid was added as a dispersing agent at 1.2 wt.% relative to the solid content of the suspension. Subsequently, ceramic powders (either pure Al_2O_3 or the Al_2O_3 + TiN mixture) were added to the respective liquid phase under continuous stirring with the ratios as listed in Table 1. After the addition of the powder, the suspensions were stirred at 2000 rpm for 30 minutes, followed by ultrasonic dispersion at 100% amplitude for 1 min to ensure a homogeneous particle distribution. Subsequently, the suspensions were sieved using a 45-µm mesh to remove any remaining agglomerates.

Coating Deposition

A modified TopGun-G system (GTV, Luckenbach, Germany), equipped with a peristaltic suspension feed system, was utilized to spray pure Al_2O_3 and TiN/Al_2O_3 composite coatings (Ref 16). The coatings were deposited onto planar stainless steel substrates with a dimension of 50 x 50 x 3 mm, which were surface activated by grit blasting using

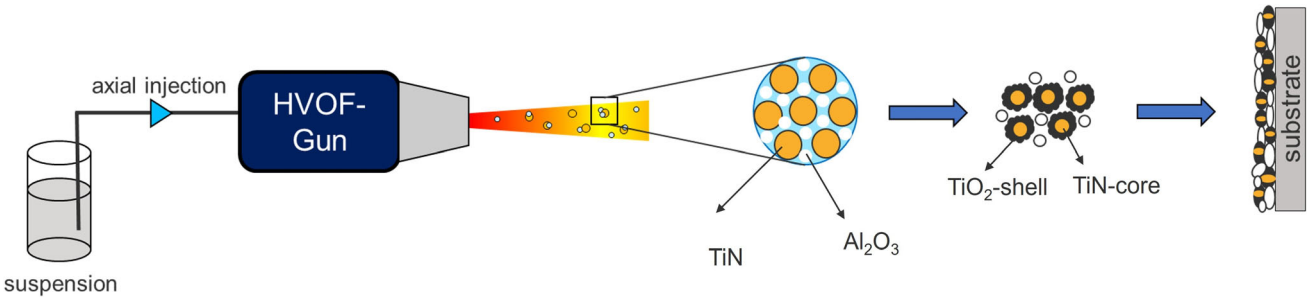

Fig. 1 SEM images of feedstock powder, (a) TiN Höganäs Grade A, (b) Al_2O_3 Martoxid MR52

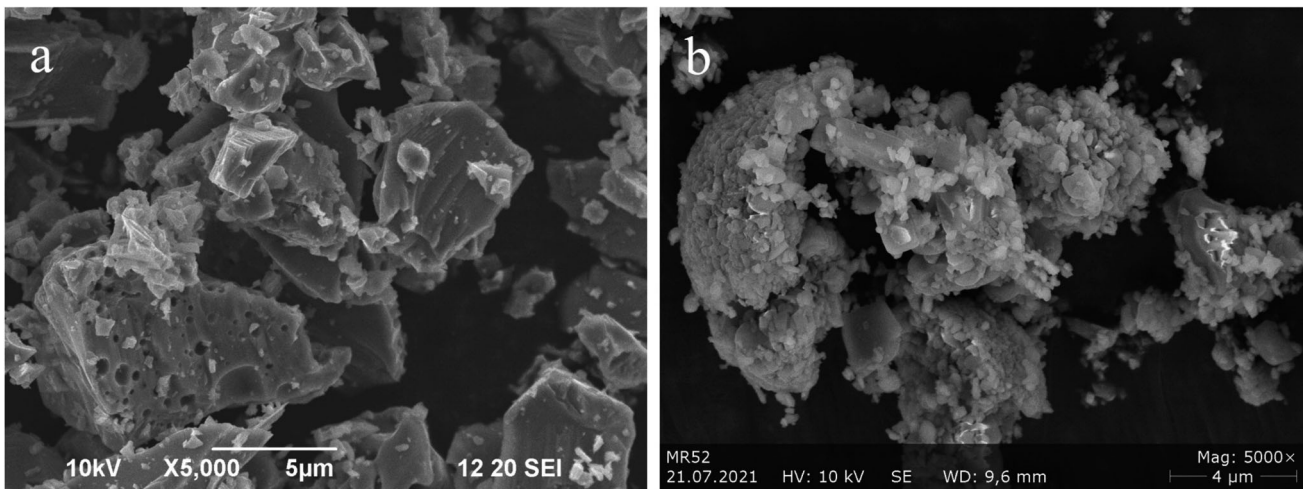

Fig. 2 Particle size distribution of the feedstock powders: (a) TiN Höganäs Grade A, (b) Al_2O_3 Martoxid MR52

Table 1 Summary of aqueous suspensions with additives used

Material	Type/manufacturer	Used additives type	Additive content, wt.%*	solid content, wt.%
Al_2O_3	MR52/Martinswerk	Polymethacrylic acid	1.7 (solid)	15
TiN/Al_2O_3 1:1	GradeA/Höganäs + MR52/Martinswerk	Hydrocolloid + polymethacrylic acid	4.0 (aqueous) 1.2 (solid)	15

*(solid) and (aqueous) indicate that the wt.% is given relative to the solid content and aqueous content, respectively.

F60 (212-300 µm) corundum at a pressure of 4 bar and then cleaned with acetone to remove residues from the surface. During the HVSFS process, the offset was set to 3 mm and the relative surface speed to 800 mm/s. In the modified torch, a suspension injector unit is installed, which allows for direct suspension injection axially into the combustion chamber. The suspension injector is equipped with a simple turbulence nozzle having an axial orifice diameter of 0.5 mm, and the suspension feed rate was set to 60 g/min. Ethene and oxygen were used as process gases in different mixtures (see Table 2), and the spray distance was kept constant at 100 mm. A schematic representation of the coating formation process is shown in Fig. 3.

Feedstock and Coating Characterization

The raw feedstock morphology and coating cross sections were examined using a scanning electron microscope (S-800, Hitachi, Japan). The particle size distribution was evaluated by laser diffraction using a Mastersizer3000 analyzer (Malvern, UK). The oxidation behavior of the TiN powder and TiN/Al_2O_3 powder mixture (1:1 wt.%) in static air was characterized by simultaneous differential thermal analysis (DTA)/ thermogravimetry (TG) using an STA 409C apparatus (Netzsch GmbH, Germany). 100 mg of each sample was heated in an alumina crucible at a rate of 10 K/min from room temperature up to 1550 °C.

Table 2 Survey of conducted spray experiments with varied spray parameters

Employed suspension, s	Coating denotation	Total gas amount, slpm	C_2H_4, slpm	O_2, slpm	Lambda, λ
S-Al_2O_3	A	284	82	202	0.82
S-TiNAl_2O_3	TA1	300	88	212	0.80
	TA2	320	94	226	0.80
	TA3	300	75	225	1.00
	TA4	320	80	240	1.00

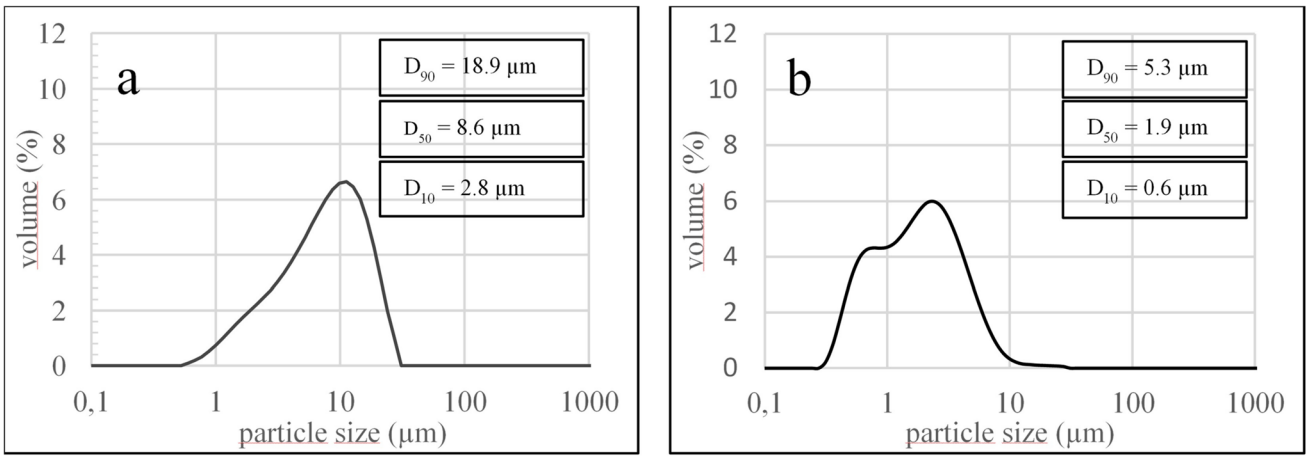

Fig. 3 Schematic description of the deposition of TiN/Al_2O_3 composite coatings

Furthermore, zeta potential measurements of the suspensions were obtained with a Zetasizer NanoZS (Malvern, UK).

The phase composition of the coatings was determined with an x-ray diffractometer (PANalytical B.V., Almelo, Netherlands) using the Cu-Kα radiation. The samples were scanned from 20 to 70° 2θ, with a step size 0.0174° and dwell time of 299.720 s. Relative fraction of the retained TiN phase was estimated based on the maximum intensities of primary diffraction peaks of TiN (200) and rutile TiO_2 (110). In order too accurately assess the degree of oxidation of the nitride particles during coating process, the calculation was normalized to the titanium containing phases, excluding the Al_2O_3 from the ratio. This approach may provide a comparative index of the TiN to rutile conversion relative to the feedstock powder.

The microstructure of the coatings was investigated on polished cross-sections prepared by grinding and polishing (Struers, US) with 15, 6, 3, and 1 μm diamond suspensions (Buehler, Germany). The microstructure of the polished cross sections was analyzed using an optical microscopy (Leica GmbH, Germany). The porosity of the coatings was evaluated using digital image analysis software (ImageJ). For each coating, five optical microscopy images were captured at a magnification of 200x to ensure statistical representativeness. The porosity values were determined using gray-level thresholding and reported as the average area percentage of these five measurements.

The hardness of the coatings was measured on polished cross sections with a Vickers indenter using a Fischerscope HM2000 testing machine (Helmut Fischer, Germany) according to DIN EN ISO 14577. The measurement was force regulated and a load of 0.1 N was applied for 20 s with a loading and release time of 5 s each. For each sample, 10 imprints on the cross section of the coating were made: The average hardness and their standard deviation were calculated.

Further microstructural analyses were carried out by transmission electron microscopy (TEM) and selected area electron diffraction (SAED) using a TALOS F200S G2 S/TEM (Thermo Fisher Scientific, Waltham, MA, USA) equipped with a Schottky field emitter operated at 200 kV and two SSDs for EDS analysis. Electron-transparent TEM samples were prepared by focused ion beam (FIB) milling using a dual-beam Helios G4 UC from FEI (now Thermo Fisher Scientific Inc., Waltham, Massachusetts, USA), equipped with a focused ion beam (FIB) of Ga^+ ions. Before FIB milling, a thin Pt layer was deposited on the film surface to prevent damage, redeposition artifacts, and Ga implantation during the milling process.

Dry Sliding Wear Test

The sliding wear performance of the coatings was evaluated according to the ASTM G99 standard in "ball-on-disk" experimental setup by tribometer (Anton Paar TriTec, Corcelles, Switzerland). Investigations were carried out using 6 mm diameter Al_2O_3 sphere as counterpart at room temperature. The surface of the samples for each composition was ground with SiC papers, then polished with 3 µm polycrystalline diamond slurry to achieve Ra < 0.1 µm, and cleaned in ultrasonic bath with acetone prior to the tests. A normal load of 10 N, a relative sliding speed of 0.10 m/s, a sliding distance of 1000 m, and a wear track radius of 7.041 mm were set as test conditions. The friction coefficient was measured by tangential force monitoring on the counterpart with a load cell and recorded during each wear test. The volume loss of the sample was assessed using a structured illumination profilometer (ConfoSurf, Confovis GmbH, Jena, Germany) mounted on an optical microscope (Nikon, Eclipse LV150N) and was converted into a specific wear rate by dividing over the sliding distance and the applied normal load. The wear loss of the spherical counterpart was assessed by measuring the diameter of the worn cap using an optical microscope (Olympus GX51). The morphology of the wear track on the coating and of the surrounding polished surface was investigated by SEM (Quanta-200, FEI), and EDX (INCA, Oxford Instruments Analytical, UK) was performed on the wear track and the polished surface to compare the respective oxide contents after the dry sliding wear test. Moreover, cross sections were obtained by metallographic cutting of worn samples, which were investigated by SEM (Helios NanoLab 600, Thermo Fisher Scientific Inc).

Results and Discussion

Feedstock and Suspension

To understand the phase stability and potential oxidation of the feedstock, the thermal behavior was first investigated under static conditions. Figure 4 shows the thermogravimetric analysis (TGA) and differential thermal analysis (DTA) curves recorded in the temperature range from 20 to 1550 °C. According to Fig. 4(a), a prominent exothermic peak appears at approximately 580 °C. At this temperature, the onset of weight gain in the TiN particles is observed, indicating the beginning of oxidation. The oxidation of TiN can proceed in two sequential steps, as described by the following reactions (Ref 17):

$$2TiN + O_2 \rightarrow 2TiON \quad \text{(Eq 1)}$$

$$2TiON + O_2 \rightarrow 2TiO_2 + N_2 \quad \text{(Eq 2)}$$

The overall reaction can be written as:

$$2TiN(s) + 2O_2(g) \rightarrow 2TiO_2(s) + N_2 \quad \text{(Eq 3)}$$

In oxygen deficient conditions, complete oxidation does not occur. Instead, partial oxidation near the particle surface leads to the formation of non-stoichiometric oxynitrides (TiO_xN_γ), typically within the temperature range of 600–900 °C (Ref 18). Above 1000 °C, a second reaction step takes place, resulting in the formation of the rutile phase of TiO_2 (Ref 17, 18). Due to the negative Gibbs free energy ($\Delta G°$), oxidation reactions are thermodynamically favorable (Ref 9).

Figure 4(b) reveals the behavior of the TiN/Al_2O_3 mixture. A notable shift in the oxidation onset temperature (from 579 to 672.7 °C) is observed, suggesting that the Al_2O_3 particles provide thermal protection for TiN particles, likely due to the shielding effect of the alumina matrix. Furthermore, the TG curve of mixture stabilizes above 1083 °C, indicating the formation of stable phase assembly under static heating conditions.

However, it is important to distinguish these static results from the HVSFS process. While DTA/TG analysis represents static oxidation process with a slow heating rate (10 K/min), the HVSFS process is characterized by high particle velocities and extremely short dwell time within the flame. Consequently, the particles are exposed to high temperatures for only a few milliseconds, which significantly limits the extent of oxidation compared to the equilibrium conditions of the thermal analysis.

Zeta potential measurements were performed to evaluate the electrostatic stability of the prepared suspensions. The Al_2O_3 suspension showed a zeta potential of – 37.73 ± 0.50 mV, while the TiN/ Al_2O_3 suspension exhibited a significantly higher absolute value of – 60.83 ± 0.98 mV. As values beyond ± 30 mV are generally considered indicative of good dispersion stability, both suspensions can be classified as stable against agglomeration. The higher absolute value in the TiN/ Al_2O_3 suspension suggests enhanced electrostatic repulsion and better suspension homogeneity.

The relatively coarse particle size of TiN was chosen intentionally to reduce its oxidation susceptibility during the high-temperature HVSFS process. Due to its lower specific surface area compared to the finer Al_2O_3 particles, TiN exhibits reduced surface reactivity in the flame. The aim is to melt the Al_2O_3 matrix while preserving a TiN core within each particle by promoting only partial surface oxidation. These TiN-core/TiO_2-shell particles can be embedded into the alumina matrix, improving bonding and microstructural integration while retaining the functional properties of TiN.

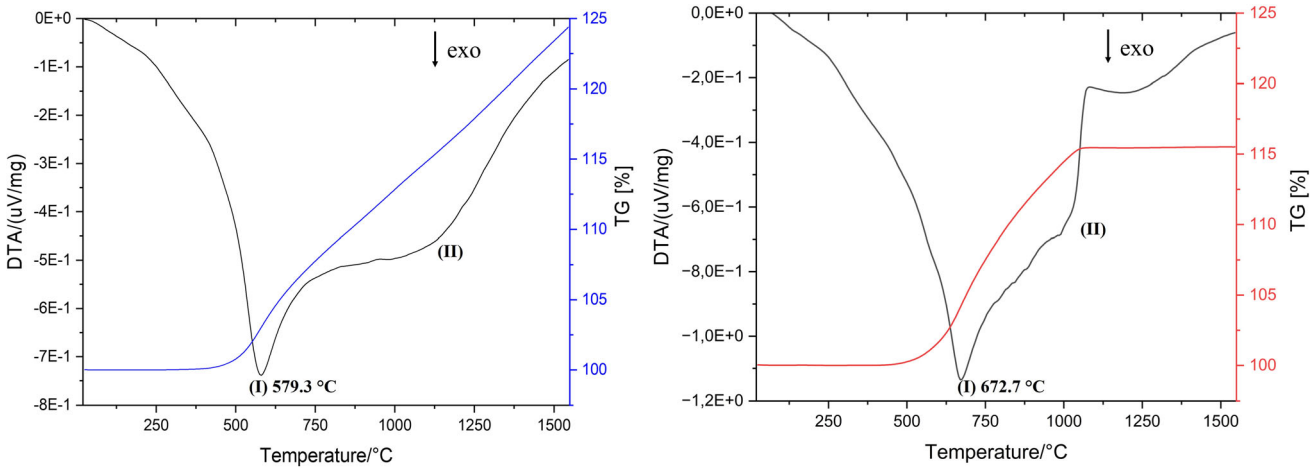

Fig. 4 DTA/TG Analysis of powders (a) TiN, (b) TiN; Al_2O_3 50:50 wt.% mixture

Microstructure and Phase Composition of As-Sprayed Coatings

Figure 5 presents light microscopy and SEM images of TiN/Al_2O_3 coating cross sections produced under varying spray parameters. In the light microscopy, the gold-brown TiN particles are clearly distinguishable within the darker alumina matrix.

For the coatings deposited under stoichiometric conditions ($\lambda = 1.0$, Fig. 5c,d), a noticeably higher fraction of light gray regions is observed in both optical and SEM (Fig. 5c2,d2) micrographs compared to the substoichiometric samples (TA1 and TA2). These light grays are attributed to oxidation products of TiN, particularly the formation of rutile, indicating an increased degree of oxidation due to the higher oxygen availability in the flame. SEM images reveal that angular unmelted TiN particles are embedded within a surrounding molten slightly darker matrix phase, as observed in BSE mode.

Furthermore, coatings deposited using a lower total gas flow (Fig. 5a,c) exhibit more frequent break-outs. These defects, most likely introduced during metallographic preparation, suggest weaker mechanical interlocking and/or reduced interfacial adhesion between the TiN particles and the surrounding, which can be attributed to the lower particle kinetic energy and impact velocity.

X-ray diffraction (Fig. 6) confirmed the presence of TiN particles through distinct TiN (111) and (200) reflections at 36.67° and 42.60°, respectively. Samples sprayed with stoichiometric gas ratios (TA3 and TA4) displayed additional peaks corresponding to rutile TiO_2, with broader features suggesting amorphous phase formation. Substoichiometric coatings showed higher TiN signal intensity and lower TiO_2 content.

The oxidation of TiN is assumed to begin during in-flight exposure, where surface reactions lead to the formation of an oxide shell. Upon impact with the substrate, rapid quenching occurs, which limits diffusion and favors the formation of amorphous TiO_2. The relatively low oxygen partial pressure in the reducing flame could have further promoted partial oxidation, leading to the possible formation of titanium oxynitride (TiON), which can exist in both crystalline and amorphous forms (Ref 18). The presence of TiOxNy cannot be unquestionably confirmed through the XRD patterns, since its main diffraction peaks are overlapped with those of rutile TiO_2 and TiN. However, a broad peak at approximately 62° can be attributed to overlapping contributions from TiN and TiO_xN_y phases. Its shape and width once again suggest a predominantly amorphous structure, likely associated with TiO_xN_y, since this feature appears more prominently under reducing conditions. Additionally, the broader reflections observed around 36° and 43° in stoichiometric coatings are intensified by higher oxygen content and are commonly associated with rutile TiO_2 as well as with possible contributions from TiO_xN_y, as reported in previous studies. (Ref 9, 18, 19).

The influence of the total gas flow is reflected in the intensity variation in the α- and γ-Al_2O_3 peaks. A higher gas volume promotes the transformation from α- to γ-Al_2O_3. In Fig. 6b, the x-ray diffraction pattern of the pure alumina coating (A) is compared with that of TA2, which contains the highest amount of TiN. It is clearly visible that the major phase in the pure alumina coating is γ-Al_2O_3, whereas in the TA2 coating, α-Al_2O_3 is more dominant. The presence of γ-Al_2O_3 in thermally sprayed coatings is typically attributed to the rapid cooling of molten alumina particles. The formation of γ- Al_2O_3 is thermodynamically favored during rapid solidification due to its lower activation energy relative to α- Al_2O_3 (Ref 20,21). However, in the case of TiN/ Al_2O_3 composite coating, the nucleation of α-Al_2O_3 appears to be promoted by the presence of rutile

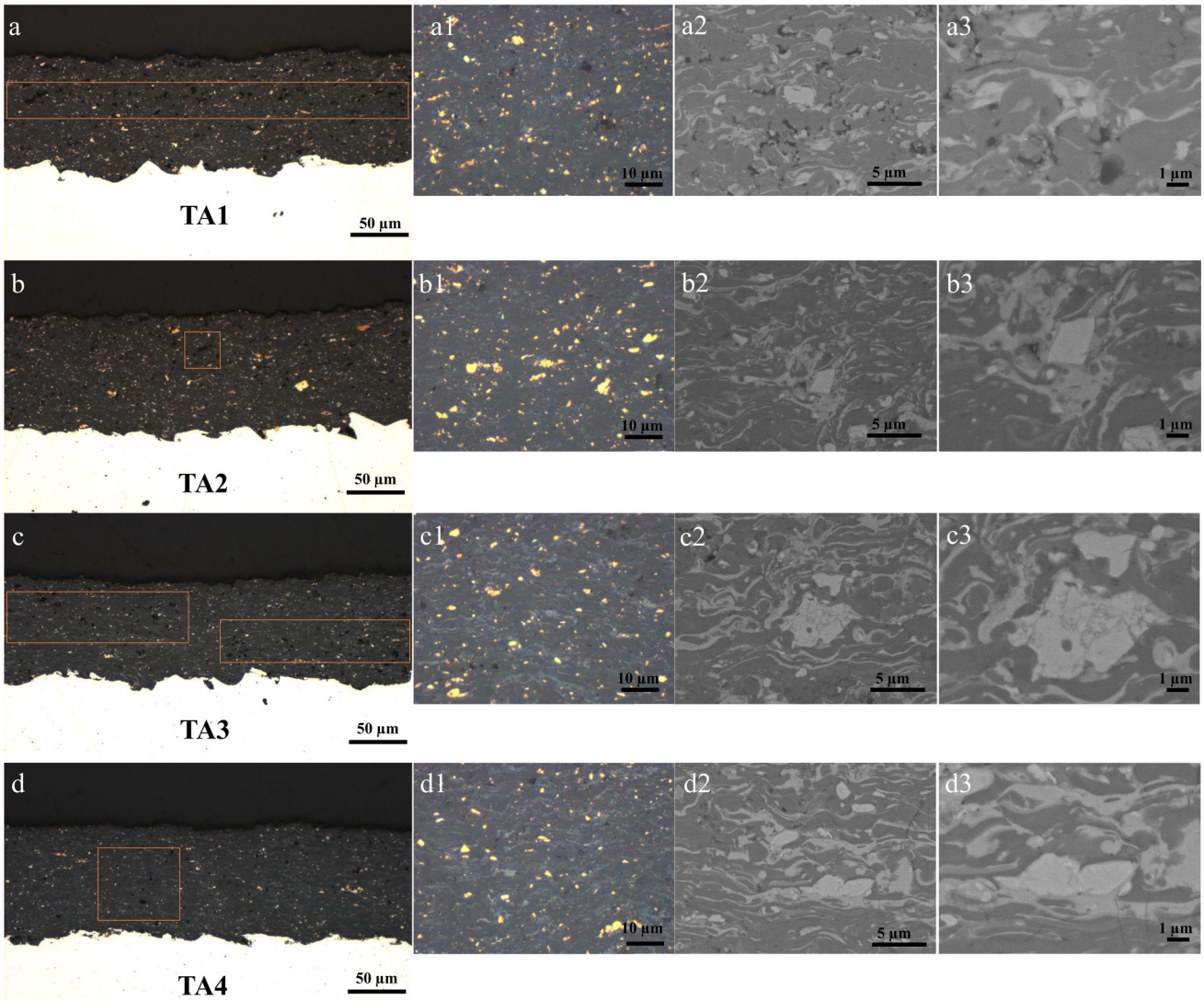

Fig. 5 Light microscopy and SEM images on cross section of TiN/Al_2O_3 coatings, deposited with different gas mix stoichiometry and total gas amount a, a1, a2, a3) λ = 0.8, total gas = 300 slpm, b, b1, b2, b3) λ = 0.8, total gas = 320 slpm, c, c1, c2, c3) λ = 1.0, total gas = 300 slpm, d, d1, d2, d3) λ = 1.0, total gas = 320 slpm

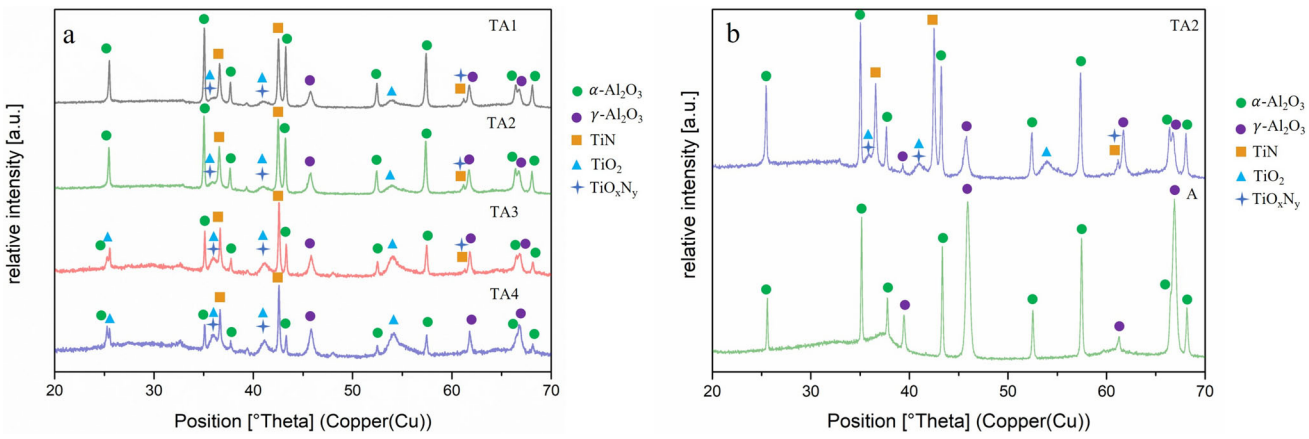

Fig. 6 X-Ray diffraction of (a) TiN/Al_2O_3 composite coatings deposited with different process parameters, (b) comparison of Al_2O_3 (A) and TA2 layers

TiO_2, which is formed in flight around the TiN particles as mentioned (Ref 9, 22).

Figure 7(a) illustrates the porosity values of the coatings, revealing a dependence on the spray parameters, and confirming the qualitative observations from the microscopy images (Fig. 5). Sample TA1 exhibits the highest porosity (~4%), which is attributed to the insufficient embedding of angular TiN particles within the alumina matrix. Increasing the total gas flow significantly densifies the structure, with both TA2 and TA4 reaching porosity values below 1.5%. The lowest porosity is observed for TA4, likely resulting from the gap-filling effect of the molten oxide phase surrounding the nitride particles, as well as from the presence of fully oxidized titanium nitride particles.

Figure 7(b) presents the retained TiN fraction in the coatings, calculated from the XRD data. The values are derived from the intensity ratio of the primary TiN(200) and rutile(110) diffraction peaks as described in Section 2.3. The first bar represents the theoretical maximum based on the feedstock composition (50 wt.%). Stoichiometric conditions ($\lambda = 1.0$) in TA3 and TA4 exhibit a pronounced reduction in TiN content to approximately 24-29%, indicating substantial oxidation to rutile during in flight. In contrast, the substoichiometric parameters ($\lambda = 0.8$) preserve significantly higher TiN fractions of approximately (~39%).

The microhardness of the coatings is shown in Fig. 7c. The Al_2O_3 (A) reference sample exhibits an average Vickers hardness value of 720 ± 55 HV0.1. According to the diagram, the TiN/Al_2O_3 composite coatings exhibit a hardness ranging from 760 to 890 HV0.1. The hardness correlates with the total gas volume and the TiN content in the coating: Substoichiometric coated layers (TA1, TA2) contain a higher TiN fraction, resulting in increased hardness than TA3 and TA4, and coatings sprayed with higher

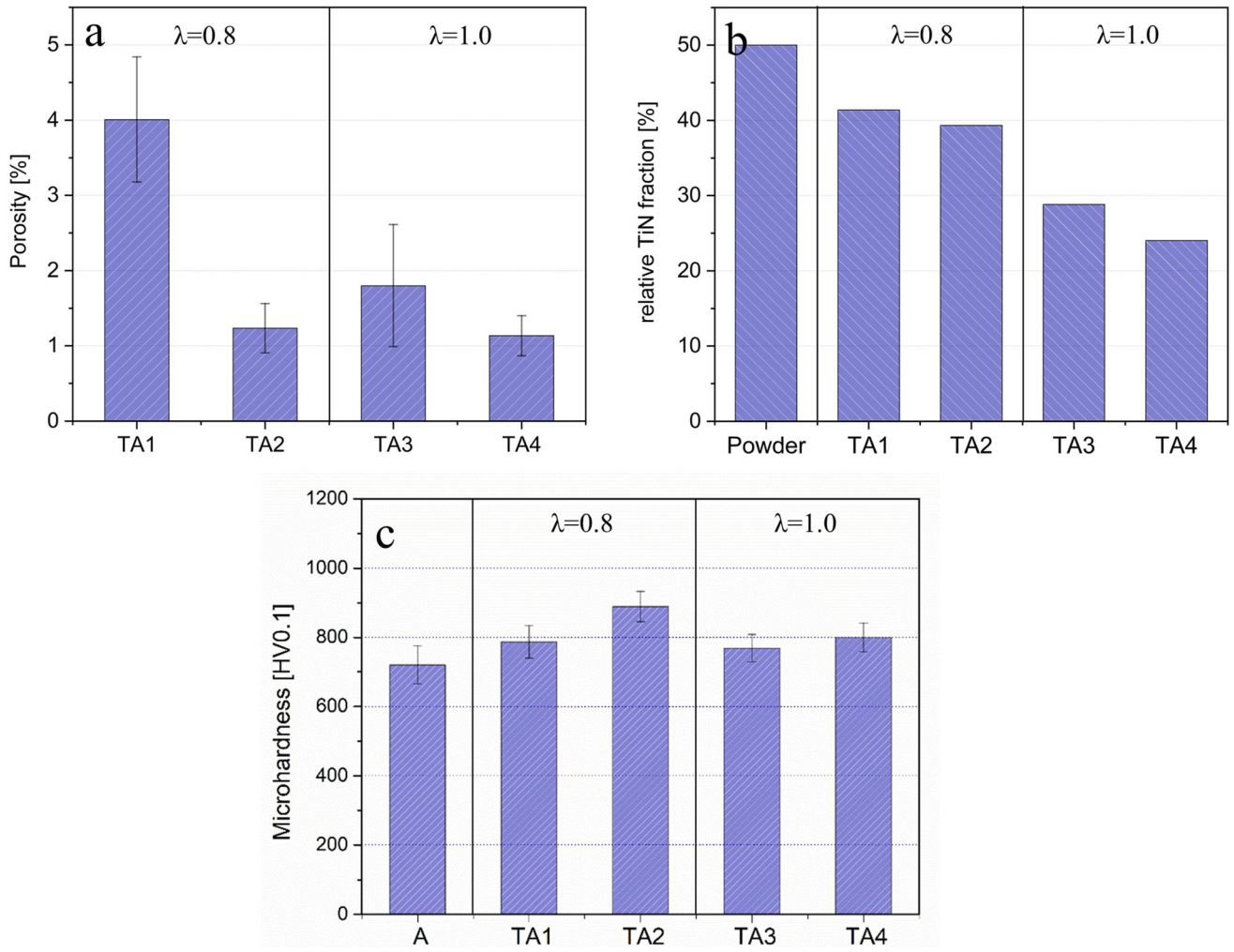

Fig. 7 Quantitative evaluation of the coating microstructure and mechanical properties. (a) Porosity determined by optical image analysis (ImageJ), (b) relative retained TiN phase fraction calculated from XRD peak intensity ratios, normalized to the initial feedstock powder, (c) Vickers microhardness of the TiN/Al_2O_3 composite coatings, deposited with different coating parameters

total gas flow rates (TA2, TA4) are harder than the corresponding samples sprayed with lower gas flow rates (TA1, TA3).

Based on microstructural observations, phase composition, and mechanical properties, the coating produced with a total gas flow of 320 slpm and a stoichiometry of $\lambda = 0.8$ demonstrates the most favorable characteristics. This coating features a dense microstructure, a high volume fraction of TiN, and the highest measured hardness, making it the most promising candidate for tribological applications. Consequently, this coating was selected for further microstructural evaluation using TEM.

The STEM micrograph (Fig. 8a) and the corresponding EDX maps (Fig. 8a1-a4) reveal a core–shell structure, where TiN cores are surrounded by oxidized shells, embedded in an Al_2O_3 matrix. Bright-field TEM details of a TiN particle with its oxidized shell (Fig. 8b, c) confirm the presence of crystalline TiN, with its lattice planes clearly identifiable in the digital zoom of Fig. 8c2: The 2.44 Å spacing corresponds to the (111) lattice planes of TiN, as corroborated by the FFT pattern in the inset. The surrounding oxide has much lower crystallinity: nanometer-sized crystalline domains, some of which are circled in Fig. 8c1, contain numerous lattice defects (e.g., dislocations), and are surrounded by low-angle grain boundaries and amorphous areas. The structural identification in these areas is more difficult, but at least some of the spots in the FFT pattern can be indexed to the (101) and (200) planes of the lattice of rutile (Fig. 8c2), consistent with the XRD patterns.

The element maps in Fig. 8a2-a4 indicate that the Ti-rich areas also exhibit some nitrogen signal accompanied by a reduced oxygen signal. This may suggest the formation of a titanium oxynitride (TiO_xN_y) phase at the interface, in addition to rutile TiO_2, as previously discussed. This shell containing rutile and TiO_xN_y might have formed during exposure of the particles to the substoichiometric flame, where, due to the incomplete combustion of ethene, carbon monoxide (CO) and hydrogen (H_2) act as reducing agents and promote the formation of TiO_xN_y as an oxidation intermediate of TiN under oxygen-deficient conditions. The formation of TiO_xN_y is thermodynamically favored, as already reported in the literature (Ref 17-19, 23, 24). The TiO_xN_y compound in the shell, if present, could be expected to improve the interfacial bonding and mechanical connection of TiN particles within the alumina matrix.

However, it should be noted that the Kα line of nitrogen is overlapped by the L-lines of Ti. While a strong nitrogen signal in the TiN cores clearly indicates the presence of nitrogen, weaker signals in titanium oxide regions may partially result from spectral overlap. Nonetheless, a localized decrease in the oxygen signal, coinciding with minor nitrogen presence, suggests the possible incorporation of nitrogen into the TiO_2 lattice via partial oxygen substitution.

Selected area electron diffraction (SAED) patterns (Fig. 8c3, c4) were evaluated based on measured interplanar spacings (d-values) and the orientation of the diffraction rings relative to the grain structure. These d-values were compared with XRD results to identify the corresponding crystallographic phases. However, the significant overlap in d-spacings among TiO_2, TiN, and TiO_xN_y complicates unambiguous phase identification by SAED or XRD. Based on the SAED and FFT analyses, the TEM results suggest that any TiOxNy present is likely contained in the amorphous areas between the nanometric rutile crystals, making its detection by diffraction based methods particularly difficult.

Wear Resistance

The coefficient of friction (CoF) of the Al_2O_3 reference coating (A) and the composite coatings TA2 and TA4 as a function of sliding distance is shown in Fig. 9(a). Initially, pure alumina and TA2 exhibit a comparable CoF values, which increases progressively with increasing sliding distance. For the TA2 coating, the CoF reaches approximately 0.6 after 100 m and then stabilizes. In contrast, the pure Al_2O_3 coating shows a more gradual increase, eventually reaching values between 0.7 and 0.8. These values are in a similar range to those reported in previous studies (Ref 25, 26). Since the coating surfaces were pre-polished, the initially smooth surfaces result in a low friction coefficient at the beginning of the dry sliding wear test. Conversely, TA4 coating exhibits an initial CoF spike at the beginning of the wear test followed by a gradually decrease with increasing sliding distance, stabilizing after approximately 400 m at values comparable to those of pure alumina coating and Al_2O_3/TiO_2 coatings reported work by Kumar et al. at room temperature (Ref 27).

The specific wear rates of the coating and their corresponding counterparts, measured as described in Section 2.4, are presented in Fig. 9(b). The Al_2O_3 reference coating (A) exhibits a wear rate of $6.2\text{x}10^{-7}$ $mm^3/(N.m)$, while the corresponding ball wear rate is about one order of magnitude lower. Compared to the reference coating, TA2 shows a further reduction in both coating and ball wear rates, reaching values of $3.07\text{x}10^{-7}$ and $1.63\text{x}10^{-9}$ $mm^3/(N.m)$, respectively. The observed increase in wear resistance may be attributed to the combined effects of increased coating hardness, reduced porosity, and higher retained TiN fraction under substoichiometric spraying conditions. In contrast, the TA4 coating exhibits significantly higher wear rate of approximately $4.44\text{x}10^{-5}$ $mm^3/(N.m)$, accompanied by increased wear of the counterpart.

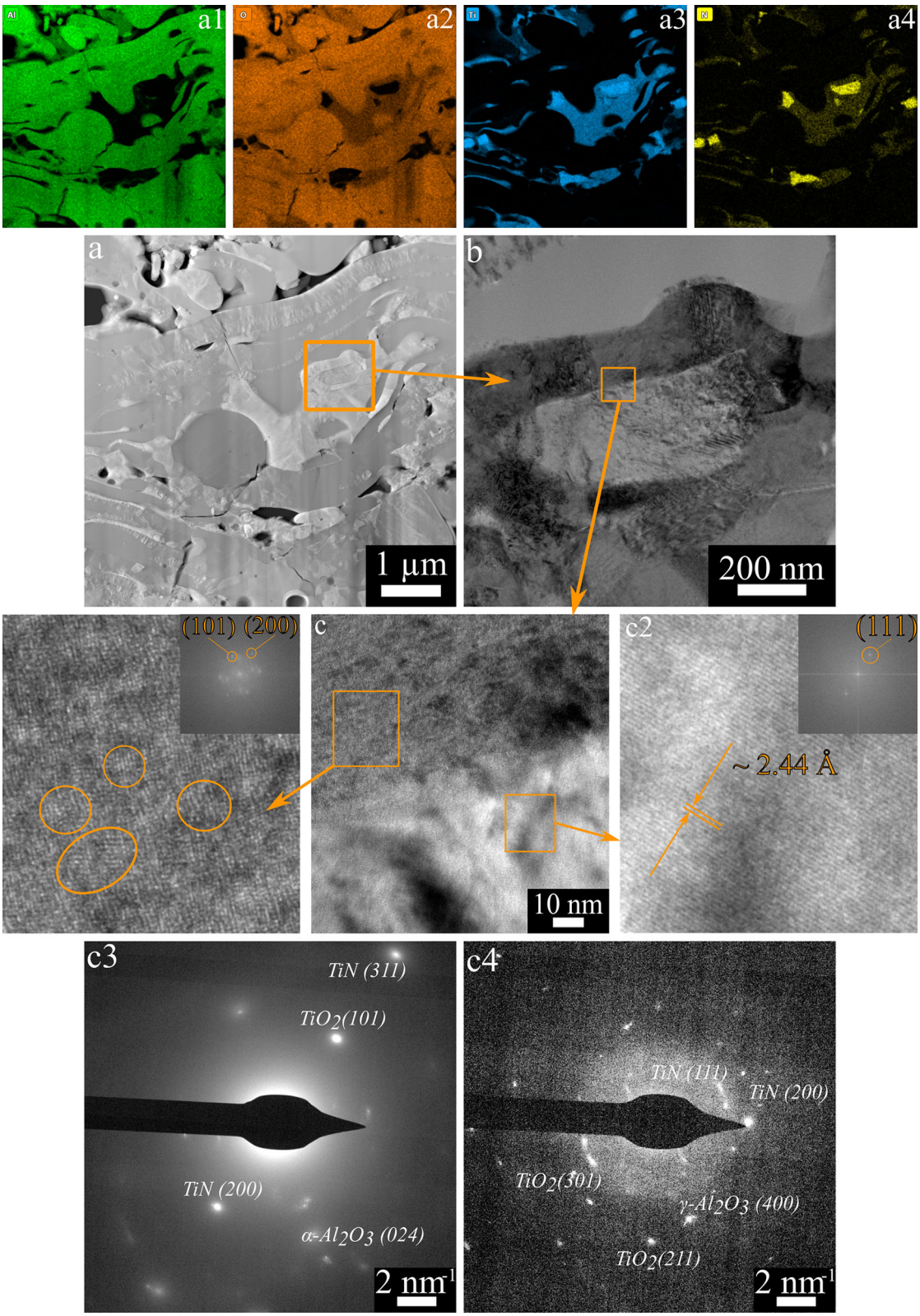

Fig. 8 High-Angle Annular Dark Field (HAADF) STEM micrograph if the TA2 sample (a) with corresponding EDX maps of Al (a1), O (a2), Ti (a3), and N (a4), bright-field TEM micrograph showing a detail of the area around a TiN particle (b), and high-resolution (HR)-TEM micrograph of the interface between the TiN particle and the surrounding oxide (c), with digital magnifications of the two marked areas (c1, c2), the corresponding FFT patterns as insets, with labeling of the signal to identifiable lattice planes of rutile (c1) and TiN (c2) and SAED patterns acquired from the respective areas (c3, c4)

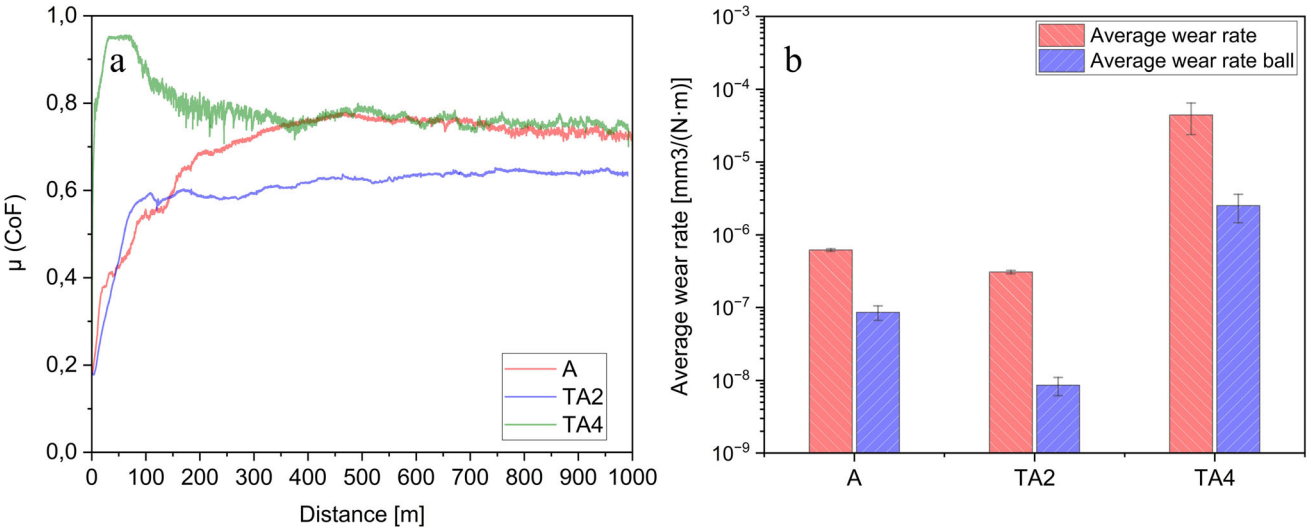

Fig. 9 (a) Coefficient of friction (μ) of the coatings measured during dry sliding wear tests, (b) wear rates of the pure alumina (A) and TiN/Al_2O_3 composite coatings (TA2 and TA4) and their respective counterparts

However, this value is comparable to wear rates reported in the literature for alumina-titania coatings (Ref 27, 28). This suggests that at $\lambda = 1.0$, the tribological behavior is governed by the extensive oxidation of TiN.

SEM images of the worn surfaces after the dry sliding wear test (Fig. 10b, e, h) reveal significant differences between the coatings. The wear scar on the Al_2O_3 coating indicates brittle fracture and spallation, which lead to the formation of cracks around the contact area. The cross section of the wear scar shows that the debris released by spallation results in the formation of a tribofilm. The occurrence of spallation is confirmed by cracks that propagate into the coating microstructure. It is inferred that brittle fracture under the applied contact stress is the primary wear mechanism of the Al_2O_3 coating, resulting in the release of debris that has a secondary abrasive action on the coating itself as well as on the counterpart, where abrasive grooves are also visible (Fig. 10a). The friction curve of Figure 9a likely attained the steady state once equilibrium was reached between the spallation process and the formation of the tribofilm.

In the case of the TA2 composite coating, shallow abrasive grooves are optically visible inside wear scar (Fig. 10e, e1), but no spallation is observed on the worn surface. However, some particles, likely TiN, appear to have been pulled out. These were probably responsible for the abrasive action on the coating itself and the counterpart (Fig. 10g). The absence of major spallation evens, in any case, resulted in a smaller amount of debris, which resulted in a significantly lower wear of the counterpart, consistent with the results plotted in Fig. 9(b). Alumina debris from the coating itself and the counterpart is embedded in the pits left by the pull-out of the TiN particles. Microcracks are visible in some of the embedded debris. In the cross section of the wear scar, a very thin tribofilm can be observed (Fig. 10f1,f2), which appears to have undergone slight spallation. The cracks are predominantly horizontal, and no crack propagation into the coating itself is observed, corroborating the previous observations on the absence of major spallation events in the TA2 composite coating.

The wear behavior of the TA4 composite coating (Fig. 10g-i) differs significantly. The worn surface (Fig. 10h) exhibits severe damage, characterized by deep abrasive grooves and extensive debris accumulation. Unlike TA2, the high magnification image (Fig. 10h1) reveals a fractured surface dominated by the pronounced pull-out of agglomerated TiN particles. These detached particles likely act as third-body abrasives, leading to the extensive wear observed on the counterpart (Fig. 10g). This degradation is primarily initiated by the detachment of weakly bonded TiN agglomerates. Due to their size and insufficient surface contact with the matrix material, these agglomerates fail to develop the necessary interfacial oxidation for effective bonding, acting as stress concentration sites. Additionally, extensive smearing of the surface on oxide matrix is observed. This behavior is attributed to the presence of the amorphous TiO_2 (as indicated in Fig. 8), which facilitates plastic flow and deformation under sliding contact.

Cross sections show (Fig. 10i, i1) a substantially wider wear track compared to TA2. Although the penetration depth is not disproportionately high, the large width of the wear scar accounts for the high volume of material loss reported in Fig. 9b. This widening suggests a rapid increase in the real contact area due to the reduced wear resistance of the coating. Furthermore, severe subsurface cracking is

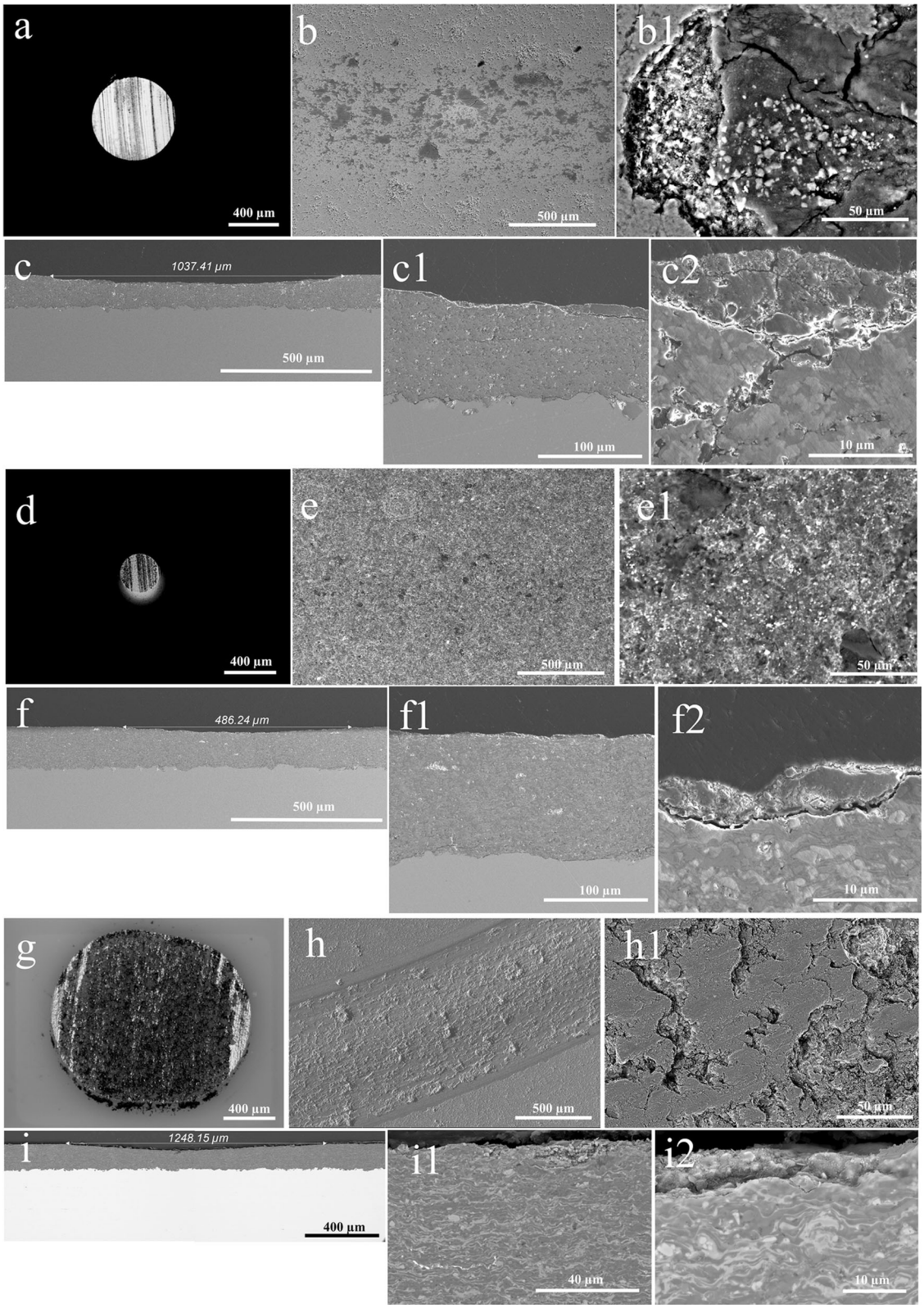

Fig. 10 (a) Al_2O_3 counterpart after the ball-on-disc test on the reference sample; (b,b1) SEM images of the wear scar on the Al_2O_3 (A) coating; (c, c1, c2) Cross-sectional SEM images of the wear scar on the Al_2O_3 coating; (d) Al_2O_3 counterpart after the ball-on-disc test on TA2; (e, e1) SEM images of the wear scar on the TA2; (f, f1, f2) cross-sectional SEM images of the wear scar on the TA2 composite coating; (g) Al_2O_3 counterpart after the ball-on-disk test on TA4; (h, h1) SEM images of the wear scar on the TA4; (i, i1, i2) cross-sectional SEM images of the wear scar on the TA4 composite coating

visible (Fig. 10i2), with cracks propagating parallel to the surface, indicative of delamination, and structural degradation associated with the weak cohesion of the agglomerates.

Conclusions

In this study, TiN/Al_2O_3 composite coatings were successfully deposited using high-velocity suspension flame spraying (HVSFS) from aqueous suspensions containing a 50:50 wt.% mixture of TiN and Al_2O_3 powders. The coatings were analyzed with respect to their microstructure, phase composition, and mechanical and tribological properties. The main findings can be summarized as follows:

- TiN/Al_2O_3 composite coatings can be directly fabricated under atmospheric conditions without the need for in situ TiN formation.
- Partial oxidation of TiN particles is favorable to achieve their incorporation into the coating.
- Sub-stoichiometric flame conditions reduce TiN oxidation and increase the retained TiN content within the coating.
- The coating sprayed with a fuel to oxygen ratio (λ) of 0.8 and a total gas flow rate of 320 slpm exhibited the highest microhardness, which is attributed to the combined effects of increased TiN retention, reduced porosity, and enhanced coating densification among all tested parameter sets.
- XRD analysis revealed a dominant presence of the α-Al_2O_3 phase in the composite coatings, whereas pure alumina coatings primarily consisted of the γ-Al_2O_3 phase. The presence of TiN and rutile TiO_2 appears to promote the formation of α-Al_2O_3.
- TEM analysis confirmed a TiN core and oxide shell structure. Around the TiN core, a nanocrystalline and amorphous interfacial oxide phase based on rutile, possibly involving nitrogen incorporation, was formed. This interfacial phase can enhance bonding between unmolten TiN particles and the alumina matrix.
- The TA2 composite coatings demonstrated significantly improved wear resistance compared to pure alumina coatings, with a tenfold reduction in counter-body wear.
- In contrast, stoichiometric conditions (λ = 1.0) resulted in lower wear resistance. This behavior is attributed to the extensive oxidation of TiN into a mostly amorphous TiO_2 phase and the weak cohesion of unmelted TiN agglomerates.
- Overall, the results indicate that the flame stoichiometry is a key parameter governing the tribological behavior of the TiN/Al_2O_3 composite coatings by controlling phase composition, oxidation degree, and microstructural characteristics.

This study demonstrates that titanium nitride (TiN) can be processed by HVSFS under atmospheric conditions without complete oxidation, despite its relatively low oxidation temperature. These findings highlight the potential of HVSFS for incorporating non-oxide phases such as nitrides into ceramic matrices, enabling the design of composite coatings with tailored properties. Under optimized coating process conditions, HVSFS-sprayed TiN-containing composite coatings offer a promising alternative for tribological applications.

Author Contributions Ebru Gyoktepeliler Akin involved in writing—original draft, visualization, validation, methodology, investigation, formal analysis, data curation, conceptualization. Luca Bortolotti took part in validation, investigation, data curation, writing—review and editing. Edoardo Rossi took part in investigation, data curation. Milena Pazzi took part in investigation, data curation. Andreas Killinger involved in resources, project administration, writing—review and editing. Luca Lusvarghi involved in writing—review and editing, project administration. Giovanni Bolelli took part in writing—original draft, writing—review and editing, visualization, project administration, investigation.

Funding Open Access funding enabled and organized by Projekt DEAL. The SEM (FEI Helios NanoLab 600) used in this was funded by the Deutsche Forschungsgemeinschaft (DFG, German Research Foundation)—project number 154585072.

Supplementary Information The online version contains supplementary material available at https://doi.org/10.1007/s11666-026-02208-3.

References

1. J.N. Musher and R.G. Gordon, Atmospheric Pressure Chemical Vapor Deposition of TiN from Tetrakis(dimethylamido)Titanium and Ammonia, *J. Mater. Res.*, 1996, **11**, p 989–1001. https://doi.org/10.1557/JMR.1996.0124
2. M.S. El-Eskandarany, Reactive Ball Milling for Fabrication of Metal Nitride Nanocrystalline Powders, Nanotechnology, *Mater. Sci. Powder Metallurg.*, 2015 https://doi.org/10.1016/B978-1-4557-7752-5.00008-5

3. M. Stoiber, M. Panzenböck, C. Mitterer, and C. Lugmair, Fatigue Properties of Ti-based Hard Coatings Deposited onto Tool Steels, *Surf. Coat. Technol.*, 2001, **142–144**, p 117–124. https://doi.org/10.1016/S0257-8972(01)01220-8
4. P. Motte, M. Proust, J. Torres, Y. Gobil, Y. Morand, J. Palleau, R. Pantel, and M. Juhel, TiN-CVD Process Optimization for Integration with Cu-CVD, *Microelectron. Eng.*, 2000, **50**, p 369–374. https://doi.org/10.1016/S0167-9317(99)00304-4
5. Q. Yang, Wear Resistance and Solid Lubricity of Molybdenum-Containing Nitride Coatings Deposited by Cathodic Arc Evaporation, *Surf. Coat. Technol.*, 2017, **332**, p 283–295. https://doi.org/10.1016/j.surfcoat.2017.10.026
6. T. Bacci, L. Bertamini, F. Ferrari, F.P. Galliano, and E. Galvanetto, Reactive Plasma Spraying of Titanium in Nitrogen Containing plasma Gas, *Mater. Sci. Eng.*, 2000, **A283**, p 189–195. https://doi.org/10.1016/S0921-5093(00)00704-8
7. W. Feng, D. Yan, J. He, X. Li, and Y. Dong, Reactive Plasma Sprayed TiN Coating and its Tribological Properties, *Wear*, 2005, **258**, p 806–811. https://doi.org/10.1016/j.wear.2004.09.057
8. J. Ma, D. Yan, J. Hu, X. Zhang, and Y. Li, Reactive HVOF Sprayed TiN-Matrix Composite Coating and its Corrosion and Wear Resistance Properties, *Trans. Nonferrous Met. Soc. China*, 2013, **23**, p 1011–1018.
9. J. Sun, C. Liu, K. Zhang, F. Venturi, A.R. Romero, and T. Hussain, TiN/TiO_2 Composite Coatings: Preparation, Microstructures and Tribological Properties, *Ceram. Int.*, 2024, **50**(18), p 32490–32504. https://doi.org/10.1016/j.ceramint.2024.06.057
10. M. Blum, E. Gyoktepeliler-Akin, and A. Killinger, High Velocity Suspension Flame Spraying of AlN/Al_2O_3 Composite Coatings, *Surf. Coat. Technol.*, 2022, **441**, p 128588. https://doi.org/10.1016/j.surfcoat.2022.128588
11. Kyocera Fineceramics GmbH. – Al_2O_3. Kyocera Solutions. https://shop.kyocera-solutions.de/storage/downloads/kyocera-f997-al2o3-deutsch.pdf Accessed May 15, 2025
12. B. Hussong, *Bedarfsgerechtes Spritzen WC-basierter HVOF-Cermet-Schichten*, Vulkan Verlag, 2016.
13. A. Förg, A. Myrell, A. Killinger, and R. Gadow, Suspension and Coating Characterization of High Velocity Suspension Flame Sprayed (HVSFS) Mixed Titanium Oxide–Titanium Carbide Coatings, *Surf. Coat. Technol.*, 2019, **371**, p 90–96. https://doi.org/10.1016/j.surfcoat.2018.08.085
14. A. Förg, M. Blum, A. Killinger, J.A. Moreno Nicolas, and R. Gadow, Deposition of Chromium Oxide-Chromium Carbide Coatings Via High Velocity Suspension Flame Spraying (HVSFS), *Surf. Coat. Technol.*, 2018, **351**, p 171–176. https://doi.org/10.1016/j.surfcoat.2018.07.072
15. P. Puddu, S. Popa, G. Bolelli, P. Krieg, M.L. Gualtieri, L. Lusvarghi, A. Killinger, and R. Gadow, Suspension HVOF Spraying of TiO_2 using a Liquid-Fueled Torch, *Surf. Coat. Technol.*, 2018, **349**, p 677–694. https://doi.org/10.1016/j.surfcoat.2018.06.062
16. A. Killinger, M. Kuhn, and R. Gadow, High-Velocity Suspension Flame Spraying (HVSFS), a New Approach for Spraying Nanoparticles with Hypersonic Speed, *Surf. Coat. Technol.*, 2006 https://doi.org/10.1016/j.surfcoat.2006.04.034
17. V. Vallejo-Otero, N. Crespo-Monteiro, E. Gamet, N. Ollier, C. Donnet, A. Valour, and Y. Jourlin, Advancements in Nitridation of TiO_2 Layers: Mechanisms, Techniques, and Applications for TiN Thin Films, *J. Eur. Ceram. Soc.*, 2025, **45**, p 117330. https://doi.org/10.1016/j.jeurceramsoc.2025.117330
18. H. Chen and F. Lu, Oxidation Behavior of Titanium Nitride Films, *J. Vac. Sci. Technol.*, 2005, **A 23**, p 1006–1009. https://doi.org/10.1116/1.1914815
19. M. Radecka, E. Pamula, A. Trenczek-Zajac, K. Zakrzweska, A. Brudnik, E. Kusior, N.T.H. Kim-Ngan, and A.G. Balogh, Chemical Composition, Crystallographic Structure and Impedance Spectroscopy of Titanium Oxynitride TiNxOy Thin Films, *Solid State Ion.*, 2011, **192**, p 693–698. https://doi.org/10.1016/j.ssi.2010.07.021
20. D. Goberman, Y.H. Sohn, L. Shaw, E. Jordan, and M. Gell, Microstructure Development of Al_2O_3–13wt.%TiO_2 Plasma Sprayed Coatings Derived from Nanocrystalline Powders, *Acta Mater.*, 2002, **50**, p 1141–1152. https://doi.org/10.1016/S1359-6454(01)00414-1
21. R. McPherson, Formation of Metastable Phases in Flame- and Plasma-Prepared Alumina, *J. Mater. Sci.*, 1973, **8**, p 851–858.
22. M. Michalak, F.L. Toma, L. Latka, P. Sokolowski, M. Barbosa, and A. Ambroziak, A Study on the Microstructural Characterization and Phase Compositions of Thermally Sprayed Al_2O_3-TiO_2 Coatings Obtained from Powders and Water-based Suspensions, *Materials*, 2020, **13**(11), p 2638. https://doi.org/10.3390/ma13112638
23. W. Wei, W. Zhao, G. Liu, and Z. Cao, Thermodynamic Description of the Ti–C–N–O System, *Calphad*, 2023, **80**, p 102520. https://doi.org/10.1016/j.calphad.2022.102520
24. E. Alves, A.R. Ramos, N.P. Barradas, F. Vaz, P. Cerqueira, L. Rebouta, and U. Kreissig, Ion Beam Studies of TiN_xO_y Thin Films Deposited by Reactive Magnetron Sputtering, *Surf. Coat. Technol.*, 2004, **180–181**, p 372–376. https://doi.org/10.1016/j.surfcoat.2003.10.131
25. G. Bolelli, B. Bonferroni, V. Cannillo et al., Wear Behaviour of High Velocity Suspension Flame Sprayed (HVSFS) Al_2O_3 Coatings Produced using Micron- and Nano-Sized Powder Suspensions, *Surf. Coat. Technol.*, 2010, **204**, p 2657–2668. https://doi.org/10.1016/j.surfcoat.2010.02.018
26. T.A. Owoseni, J.W. Murray, Z. Pala et al., Suspension High Velocity Oxy-Fuel (SHVOF) Spray of Delta-Theta Alumina Suspension: Phase Transformation and Tribology, *Surf. Coat. Technol.*, 2018, **371**, p 97–106. https://doi.org/10.1016/j.surfcoat.2018.08.047
27. D. Kumar, Q. Murtaza, R.S. Walia et al., Comparative Investigation on Thermally Sprayed Al_2O_3, Al_2O_3–13%(TiO_2) and Al_2O_3–40%(TiO_2) Composite Coatings from Room to 400 °C Temperature, *Surf. Topogr. Metrol. Prop.*, 2022, **10**, p 015043. https://doi.org/10.1088/2051-672X/ac5a75
28. E. Klyatskina, L. Espinosa-Fernande, G. Darut et al., Sliding Wear Behavior of Al_2O_3-TiO_2 Coatings Fabricated by the Suspension Plasma Spraying Technique, *Tribol. Lett.*, 2015, **59**, 8. https://doi.org/10.1007/s11249-015-0530-5